Onset of vacancy-mediated high activation energy leads to large ionic conductivity in two-dimensional layered Cs$_2$PbI$_2$Cl$_2$ Ruddlesden-Popper halide perovskite

Nisha Hiralal Makani [1,*] Aditi Sahoo [1,*] Pulak Pal,[2] Tufan Paul [1] Lokesh Singh Tanwar [1] Manoj Singh [1]
Aswini Ghosh [2,†] and Rupak Banerjee [1,†]

[1]*Department of Physics, Indian Institute of Technology Gandhinagar, Palaj 382355, India*
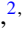[2]*School of Physical Sciences, Indian Association for the Cultivation of Science, Jadavpur, Kolkata 700032, India*

We report the dielectric properties of a two-dimensional layered Ruddlesden-Popper halide perovskite Cs$_2$PbI$_2$Cl$_2$ synthesized via a simple mechanochemical process to explore fundamental aspects of ionic conduction and relaxation mechanism over a wide temperature and frequency range. Several experimental techniques, such as complex impedance spectroscopy, alternating current (AC) conductivity spectroscopy, and complex electric modulus spectroscopy, have been employed to investigate the nuances of ionic conduction and relaxation mechanisms, and the results have been corroborated using different theoretical models, such as the Maxwell-Wagner equivalent circuit model, the modified Jonscher power law, the Havrilliak-Negami (HN), and the Kohlrausch-Williams-Watts (KWW) model. The contribution of the grains and grain boundaries to the total impedance in the system is estimated by the analysis of the Nyquist plots. In temperature-dependent AC conductivity spectra, a critical temperature (413 K) is observed, beyond which the conductivity increases abruptly. This critical temperature also defines two distinct temperature ranges: the low-temperature (303–413 K) and the high-temperature (423–463 K) regimes, where the ionic transport mechanism switches from the normal ionic transport to a vacancy-mediated ionic transport mechanism. A substantially high activation energy $\sim$1.82 ($\pm$0.02) eV is calculated from the Arrhenius plot of the ionic conductivity in the high-temperature region, while at the low-temperature region, the activation energy is found to be $\sim$0.48 ($\pm$0.02) eV. The abrupt jump in the ionic conductivity beyond the critical temperature is attributed to the onset of the anionic vacancy-mediated enhanced ionic conductivity. Polaronic models have been used to interpret the AC conductivity and its power-law exponent. The activation energy obtained from ionic conductivity measurements is consistent with those calculated from relaxation time using the HN and KWW models. The presence of two master curves in time-temperature superposition scaling of AC conductivity and modulus loss spectra specifies the validity of two different conduction mechanisms.

I. INTRODUCTION

In the last decade, the research associated with organic-inorganic hybrid perovskite solar cells has progressed at a phenomenal rate [1–4]. However, low stability remains a major bottleneck in their widespread deployment as commercial devices [5]. It is generally agreed that the instability or degradation of the hybrid perovskite might happen through two dominant mechanisms: the hydration or oxidation induced by moisture or oxygen and the ion migration-driven lattice breakdown [6,7]. Since the first kind of degradation is attributed to the presence of unstable organic components, methodical encapsulation of the device or substitution of the organic components with suitable inorganic monovalent cations has been used to address this issue [8]. The decomposition by the ion migration is, however, more challenging to address, but it has been demonstrated that such degradation can be suppressed to a large extent by employing the two-dimensional

(2D) Ruddlesden-Popper halide perovskites (RPHP) phases due to the favorable interconnection of the octahedral slab by large spacer cation [9,10]. These 2D RPHP structures have attracted significant interest in recent years owing to their distinctive properties, including large exciton binding energy, strong quantum confinement effects, and enhanced stability [11]. Consequently, the 2D RPHP structures have emerged as possible alternatives to their 3D analogs for high-efficiency solar cells and light-emitting diodes, exhibiting diverse and controllable optoelectronic features [12–17]. Compared to the organic-inorganic RPHP, all inorganic 2D RPHP are not only more stable but also easier to fabricate [18,19]. The generic formula of cesium and lead-based all-inorganic 2D RPHPs is Cs$_{n+1}$Pb$_n$X$_{3n+1}$ (X = halides or their mixtures, $n = 1, 2, \ldots$) where an extra CsX layer separates the n layers of CsPbX$_3$ [20]. The Cs$_2$PbI$_2$Cl$_2$, a newly developed all-inorganic 2D RPHP, exhibits excellent carrier mobility, great photo response, and outstanding stability [18]. It has a direct band gap (E_g) of 3.04 eV and is a potential material for α-particle counting [18]. This Cs$_2$PbI$_2$Cl$_2$ also demonstrates an ultralow thermal conductivity of $\sim$ 0.37–0.28 W/mK in the temperature range 295–523 K [20]. The basic understanding of ionic

conduction and dielectric relaxation mechanism of this 2D $Cs_2PbI_2Cl_2$ RPHP is still incomplete and quite challenging both from fundamental and technological perspectives.

Dielectric spectroscopy is one of the most prevalent and nondestructive techniques to investigate the conduction and relaxation mechanism of such materials [21,22]. Among other things, it is used to investigate the ionic conductivity, dynamics of energy storage, relaxation mechanism, and energy dissipation in electrochemical and solid-state devices in a large frequency and temperature range with prospective technological applications in batteries, self-powered sensors, solar cells, and other devices [23–28]. Halide perovskites are promising new-generation photovoltaic materials with high power conversion efficiency and low manufacturing cost. Nowadays, along with conducting polymers or other highly conducting materials, halide perovskites are also being extensively investigated to obtain high ionic conductivity for their uses in Li-ion batteries, dual-ion batteries, photo batteries, and other electronics [29–32]. From the dielectric response, the nonlocalized (known as long-range conductivity) and localized conduction (also known as dielectric relaxation) processes in a material can be understood, which manifest themselves by the relaxation peak being present or absent in the imaginary part of modulus data [33]. Additionally, the actual transport mechanism in a material can be recognized by the value of its activation energy and relaxation time [34]. The presence of vacancy in the material also significantly impacts its ionic transport, as reported by Zhao *et al.* [35]. Nevertheless, for widespread applications in batteries, solar cells, and photodetectors, an in-depth understanding of the conduction and relaxation mechanisms of the RPHPs is imperative.

In the present article, we have synthesized 2D $Cs_2PbI_2Cl_2$ Ruddlesden-Popper halide perovskite with a simplified mechanochemical synthesis process at ambient temperature. Since the $Cs_2PbI_2Cl_2$ is a relatively unexplored 2D RPHP, we have performed extensive dielectric measurements in a wide temperature (303–463 K) and frequency ($f = 4$ Hz to 8 MHz) range to understand the ionic conduction as well as the relaxation mechanism using different techniques such as complex impedance spectroscopy, alternating current (AC) conductivity, and complex electric modulus spectroscopy. The complex impedance spectra are explored in depth to understand the dynamics of grains and grain boundaries and their contribution to ion transport at different temperatures. In the temperature-dependent AC conductivity spectra, two distinct temperature regions are observed: one is the low-temperature region (303–413 K), and the other is the high-temperature region (423–463 K). The ionic transport mechanism in our system switches from normal ionic transport to a vacancy-mediated ionic transport mechanism. A substantially high activation energy of $\sim 1.82 \,(\pm 0.02)$ eV is also calculated from the Arrhenius plot of the ionic conductivity in the high-temperature region, while in the low-temperature region, the activation energy is found to be $\sim 0.48 \,(\pm 0.02)$ eV. The activation energies calculated from the ionic conductivity plots match closely with that extracted from the relaxation time for both temperature regions. The validity of the time-temperature-superposition principle in both temperature regimes is established by the scaling of the AC conductivity and the modulus loss spectra.

II. EXPERIMENTAL

A. Materials and chemicals

PbI_2 (98%, Sigma Aldrich) and CsCl (99%, Sigma Aldrich) were used as received without any additional purification.

B. Synthesis of $Cs_2PbI_2Cl_2$ perovskite

Mechanochemical synthesis has become a common solvent-free route to synthesizing metal halide perovskite [36–41]. To prepare $Cs_2PbI_2Cl_2$, PbI_2 (1 mmol 461 mg; 98%, Sigma Aldrich) and CsCl (2 mmol 336.72 mg; 99%, Sigma Aldrich) were loaded with a molar ratio of 1:2 and ground for 2 h using mortar pestle at ambient temperature (see Fig. S1 in the Supplemental Material [42]).

III. CHARACTERIZATIONS

A. Structural and optical characterizations

To evaluate the phase purity and crystal structure of the $Cs_2PbI_2Cl_2$ particles, x-ray diffraction (XRD) measurement was performed using a multipurpose x-ray diffractometer (Smart Lab, Rigaku Corporation, Japan). Thermogravimetric analysis (TGA) and differential scanning calorimetry (DSC) were investigated using a Netzch STA 449 F3 Jupiter to understand the thermal stability of the material. The UV-Vis absorbance spectrum (in the range 300–1000 nm) was studied using a UV-Vis NIR Carry 5000 Agilent spectrometer. The microstructural and elemental analysis of the as-prepared samples was performed using a field-emission scanning electron microscope (JEOL JSM-7900F). NEXA-based thermoscientific x-ray photoelectron spectroscopy (XPS) was used to determine the compositional analysis and the oxidation states of the prepared material.

B. Dielectric measurement

For dielectric measurement, the synthesized $Cs_2PbI_2Cl_2$ RPHP sample (powder) was pressed into a pellet using stainless steel dies with a diameter of 10 mm and a thickness of 1.01 mm. The prepared pellet was placed in a two-electrode configuration set up for dielectric measurements using an LCR spectrometer (HIOKI, model IM 3536). The measurement was carried out in the frequency range of 4 Hz to 8 MHz with a perturbation potential of 1.0 V by placing the conductivity cell in a cryostat with temperature stability of ± 0.10 K in vacuum (0.01 mbar) in the temperature range 303–463 K.

IV. RESULTS AND DISCUSSION

A. Structural properties

Figure 1(a) shows the XRD profile of as-synthesized $Cs_2PbI_2Cl_2$ with sharp and intense peaks at 16.34°, 21.05°, 22.23°, 28.27°, 31.63°, and 42.89° corresponding to the (101), (103), (110), (006), (200), and (215) planes. Rietveld refinement using FullProf software confirms that $Cs_2PbI_2Cl_2$ exhibits a tetragonal lattice system with $I4/mmm$ space group. The value of lattice cell parameters are $a = b = 5.656$ Å, $c = 19.015$ Å, and $\alpha = \beta = \gamma = 90°$. The Rietveld refinement results confirm the absence of any impurity phase within the material. Figure 1(b) shows the crystal structure of 2D $Cs_2PbI_2Cl_2$ drawn with VESTA. In this structure, the
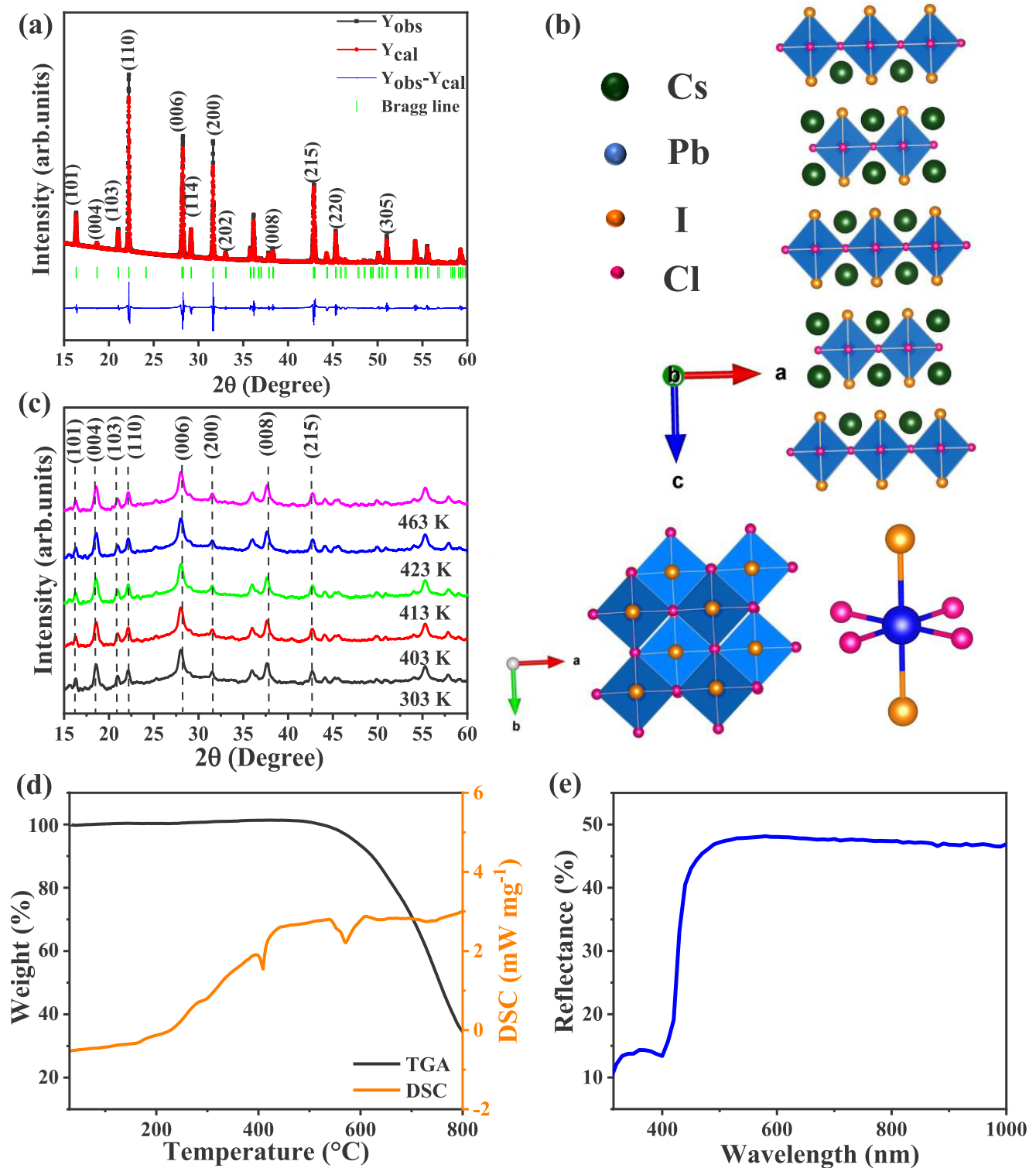
FIG. 1. (a) XRD pattern and Rietveld analysis at room temperature and (b) the ambient crystal structure along different crystallographic axes and the elongated $[PbI_2Cl_4]$ octahedral unit. (c) *In situ* temperature-dependent XRD data, (d) TGA and DSC data, and (e) reflectance spectra of the prepared $Cs_2PbI_2Cl_2$ RPHP.

two-dimensional $[PbI_2Cl_2]_n^{2n-}$ plane is made through corner-sharing Pb-centered $[PbI_2Cl_4]^{4-}$ units where Cl ions are sharing the corners by occupying the in-plane site, and I ions are situated at the out-of-plane sites serving as terminal ligands. In this structure, Cs^+ ions behave as spacer ions and balance the overall charges of the system. So $Cs_2PbI_2Cl_2$ is a RP-structured halide perovskite with a single layer ($n = 1$) [18,20]. We have performed the temperature-dependent XRD

FIG. 2. (a) FESEM image, (b) EDX spectra, and (c) elemental mapping of the synthesized $Cs_2PbI_2Cl_2$ RPHP.

[see Fig. 1(c)] but did not observe any significant changes in either the peak position, the number of peaks, or splitting of peaks as previously reported by Patru *et al.* [43]. We thus infer that no structural phase transition occurred in our 2D RP 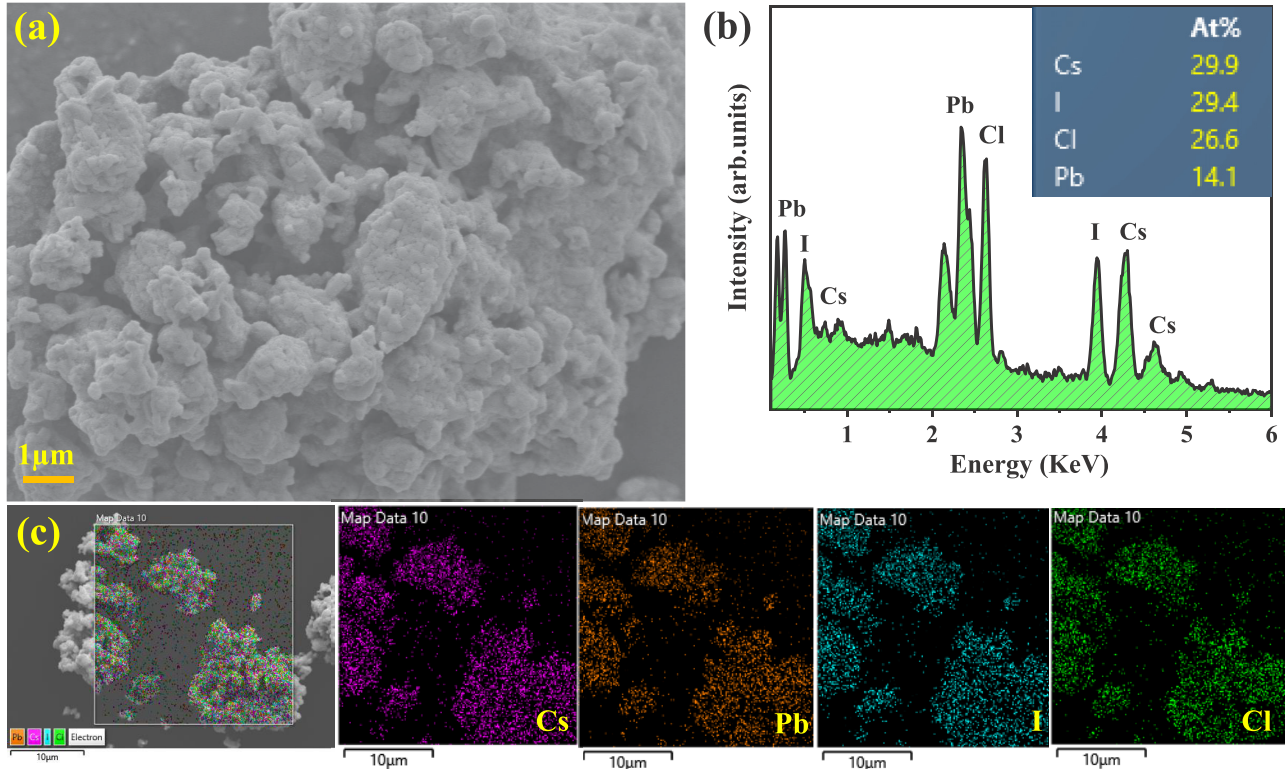$Cs_2PbI_2Cl_2$ perovskite. Additionally, we have performed two heating-cooling cycles of DSC measurement (see Fig. S2 [42]) but did not observe any exothermic or endothermic peak characteristic of a phase transition in the temperature range 303–463 K. We have also calculated the crystallite size and observed only a slight increase in the grain size in this small temperature window of 303–463 K. The TGA of the synthesized sample over a wide temperature range of 25–800 °C is shown in Fig. 1(d), which indicates that there is no weight loss until 550 °C. A sharp peak is registered at 410 °C in the DSC curve [Fig. 1(d)] due to the start of congruent melting of the material [18]. Another peak in the DSC curve at 550 °C suggests the decomposition and mass loss of $Cs_2PbI_2Cl_2$ RPHP. UV-Vis absorbance measurements were performed to calculate the band gap energy of the prepared $Cs_2PbI_2Cl_2$ powder. Figure 1(e) shows the diffuse reflectance spectra, i.e., R (%) as a function of the incident wavelength λ (nm). The band gap obtained from this curve is 3.10 eV. The band gap value is slightly higher than the reported value (~ 3.04 eV) of $Cs_2PbI_2Cl_2$ [18] and may be due to the presence of vacancies in the material [44].

Field-emission scanning electron microscopy (FESEM) image of the prepared 2D $Cs_2PbI_2Cl_2$ powder is shown in Fig. 2 with the EDX spectra and elemental mapping. The average grain size of the particles turns out to be 1–1.5 μm

in Fig. 2(a). The EDX spectra and corresponding quantitative elemental percentage shown in Fig. 2(b) reveal the deficiency of Cl ions in the prepared material compared to the actual stoichiometry envisaged that leads to Cl vacancy in the system [45]. The quantitative analysis has been performed in different regions of the material (see Figs. S3 to S7 [42]), and the atomic percentage calculation in all the regions of our sample shows sizable Cl vacancy. Figure 2(c) represents the elemental mapping of the material. The concentrations of the elements Cs, Pb, I, and Cl in the sample are mapped to provide detailed information about the overall composition of the sample. It may be noted that from the XRD at room and high temperatures (up to 463 K), no noticeable change in crystallographic structure could be identified.

XPS measurement is performed to analyze the oxidation state and elemental composition of the $Cs_2PbI_2Cl_2$ RPHP. Figure 3(a) shows a doublet peak with binding energies ~ 724.33 and ~ 738.28 eV, corresponding to the Cs $3d_{5/2}$ and Cs $3d_{3/2}$ states, respectively. Figure 3(b) shows two peaks at ~ 138.43 and ~ 143.23 eV associated with Pb $4f_{7/2}$ and Pb $4f_{5/2}$ states, respectively. Peaks observed at 618.88 eV and 630.43 eV in iodine spectra [Fig. 3(c)] correspond to I $3d_{5/2}$ and I $3d_{3/2}$ states, respectively. Deconvoluted peaks of Cl at 198.08 and ~ 199.68 eV, shown in Fig. 3(d), are associated with the Cl $3d_{5/2}$ and Cl $3d_{3/2}$ states, respectively. These results are consistent with those reported in the literature and display that all the constituent elements (Cs, Pb, Cl, and I) are in their typical valence states, which are 1^+, 2^+, 1^-, and 1^-, respectively [46].
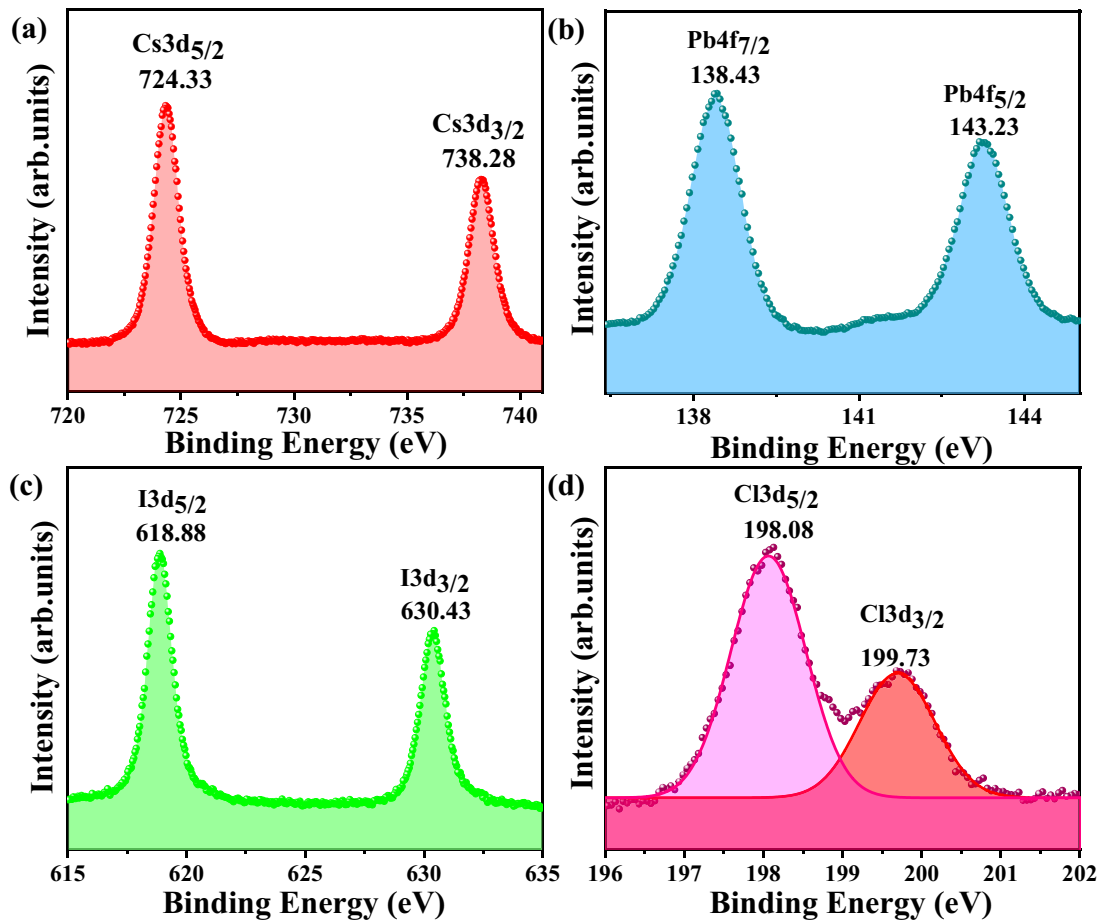
FIG. 3. XPS of (a) Cs $3d_{5/2}$ and Cs $3d_{3/2}$, (b) Pb $4f_{7/2}$ and Pb $4f_{5/2}$, (c) I $3d_{5/2}$ and I $3d_{3/2}$ (d) Cl $3d_{5/2}$ and Cl $3d_{3/2}$ of $Cs_2PbI_2Cl_2$ RPHP.

B. Analysis of complex impedance spectroscopy

Dielectric impedance spectroscopy has the unique ability to explore many of the electrical properties of materials over a broad frequency and temperature range. It provides a critical understanding of the dynamics of bound and mobile charges, energy storage, and energy dissipation processes in solid-state devices, which would reveal variations in resistance, capacitance, electrical conductivity, and relaxation time [47]. Figure 4(a) shows the variation of the real part of complex impedance $[Z'(\omega)]$ as a function of applied frequency for different temperatures between 303 and 463 K in steps of 10 K. It is observed that the value of $Z'(\omega)$ is large at low frequencies and drops as the frequency increases for all temperatures. At higher frequencies, no notable change in $Z'(\omega)$ is observed with the change in temperature, which suggests the release of space charges along with the decrease of the contribution of the grain boundaries to total impedance in the high-frequency region [48]. This change in the barrier characteristics and space charge release implies a higher value of AC conductivity for higher temperatures in the high-frequency domain which we discuss later [49]. The decrease in $Z'(\omega)$ with increasing temperature is mainly attributed to a reduction in the trapped charge density and consequent increase in the mobility of the charge carriers evidencing the combined effect of dipolar, electronic, and orientation polarization and their substantial impact on the overall impedance.

Further, the imaginary part of the complex impedance $[Z''(\omega)]$ is plotted against angular frequency (ω) in the same temperature range (303–463 K) in Fig. 4(b). This $Z''(\omega)$ vs ω, known as the loss spectrum, shows distinct relaxation peaks at various temperatures. The relaxation peak arises whenever the external field frequency matches the frequency of the localized hopping electron. The width of the relaxation curve in the $Cs_2PbI_2Cl_2$ 2D RPHP is noted to be substantially larger than that of an ideal Debye curve [50], indicating a non-Debye relaxation behavior. It is further noted that as the temperature increases, the relaxation peak moves towards a higher frequency, suggesting the presence of thermally activated charge carriers.

Figure 4(c) shows a fitted Nyquist plot or Cole-Cole plot, which is defined as the plot between the real part $Z'(\omega)$ and the imaginary part $Z''(\omega)$ of the complex impedance $Z^* = Z'(\omega) - j\,Z''(\omega)$, in the temperature range 303–363 K, for $Cs_2PbI_2Cl_2$ RPHP, and the inset shows the enlarged view of the equivalent circuit model and the circuit parameters used to fit the Cole-Cole plot. Figure 4(d) shows the fitted semicircular arcs in the temperature range from 373 to 413 K, and the inset of Fig. 4(d) shows the same in the temperature range from 423 to 463 K. For any dielectric material, the Nyquist plot typically shows three separate semicircles corresponding to the grain (high-frequency region), grain boundary (mid- to low-frequency region), and electrode-sample interface (ultra-low-frequency region) [51]. As observed in our
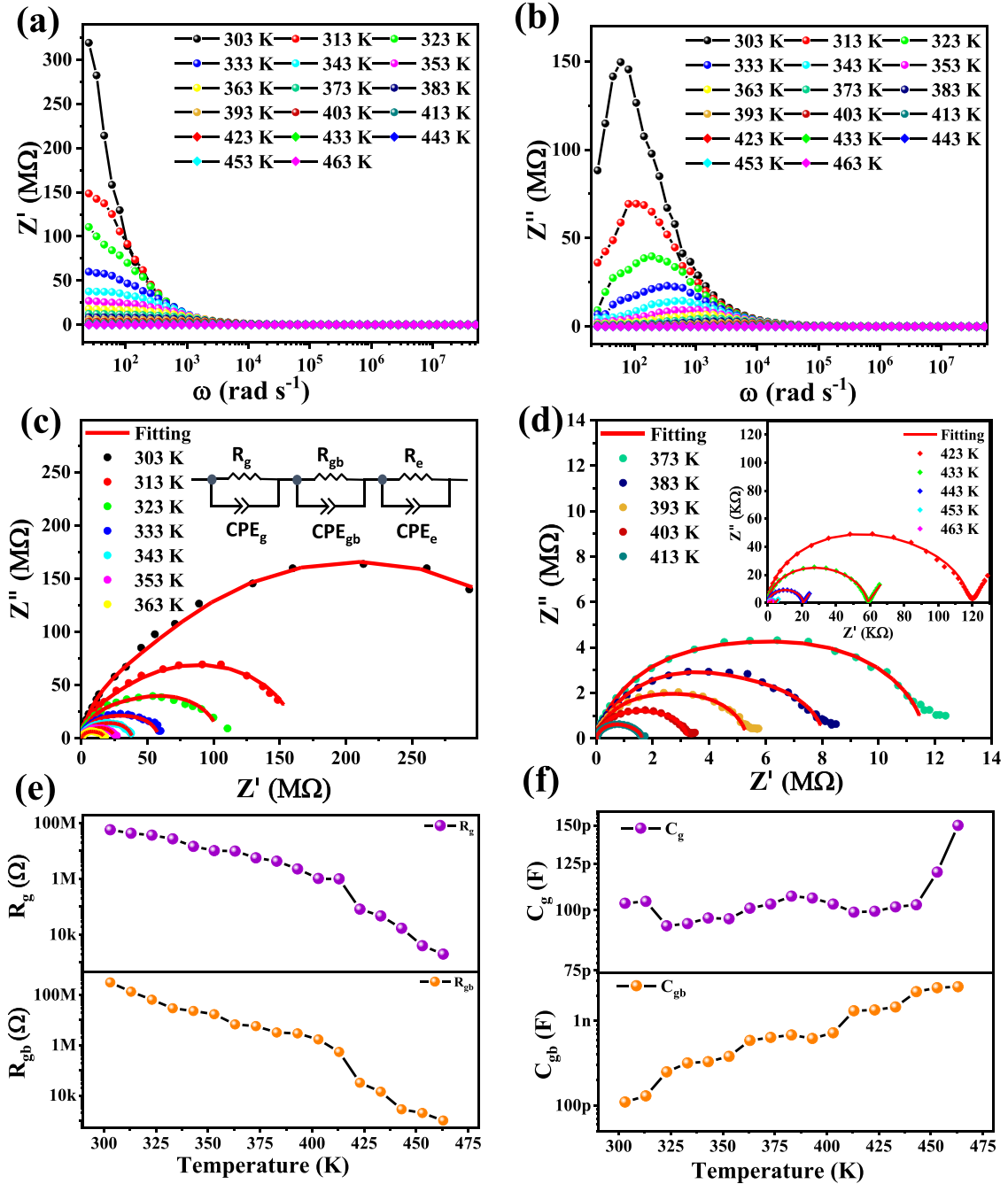
FIG. 4. (a) Frequency-dependent Z' and (b) Z'' at different temperatures. (c) The complex plane Nyquist plots of $Cs_2PbI_2Cl_2$ RPHP from 303 to 363 K; inset: the equivalent circuit model used to fit the data. (d) Similar plots for 373–413 K; inset: plots for 373–463 K. (e) The variation in the resistances R_g and R_{gb} and (f) the variation in capacitances C_g and C_{gb} over the whole temperature range, extracted from fitting the data.

system, semicircles (corresponding to different temperatures in the range of 303–463 K) are not perfect due to the superposition of the three semicircular contributions. From Figs. 4(c) and 4(d), it is observed that the semicircle diameter decreases as temperature increases, which indicates the enhancement of the ionic conductivity with the increase in temperature and non-Debye type of relaxation behavior in the sample [52]. We used the Maxwell-Wagner equivalent circuit model to distinguish the contributions of the grains, grain boundaries,

and the sample-electrode surface from the single depressed semicircle [53].

The Nyquist plots are fitted using the ZView software, which comprises three R-CPE circuits in parallel combination, where R is the resistance and CPE is the constant phase element impedance defined as

$$Z_{CPE} = \frac{1}{A(j\omega)^n}, \tag{1}$$

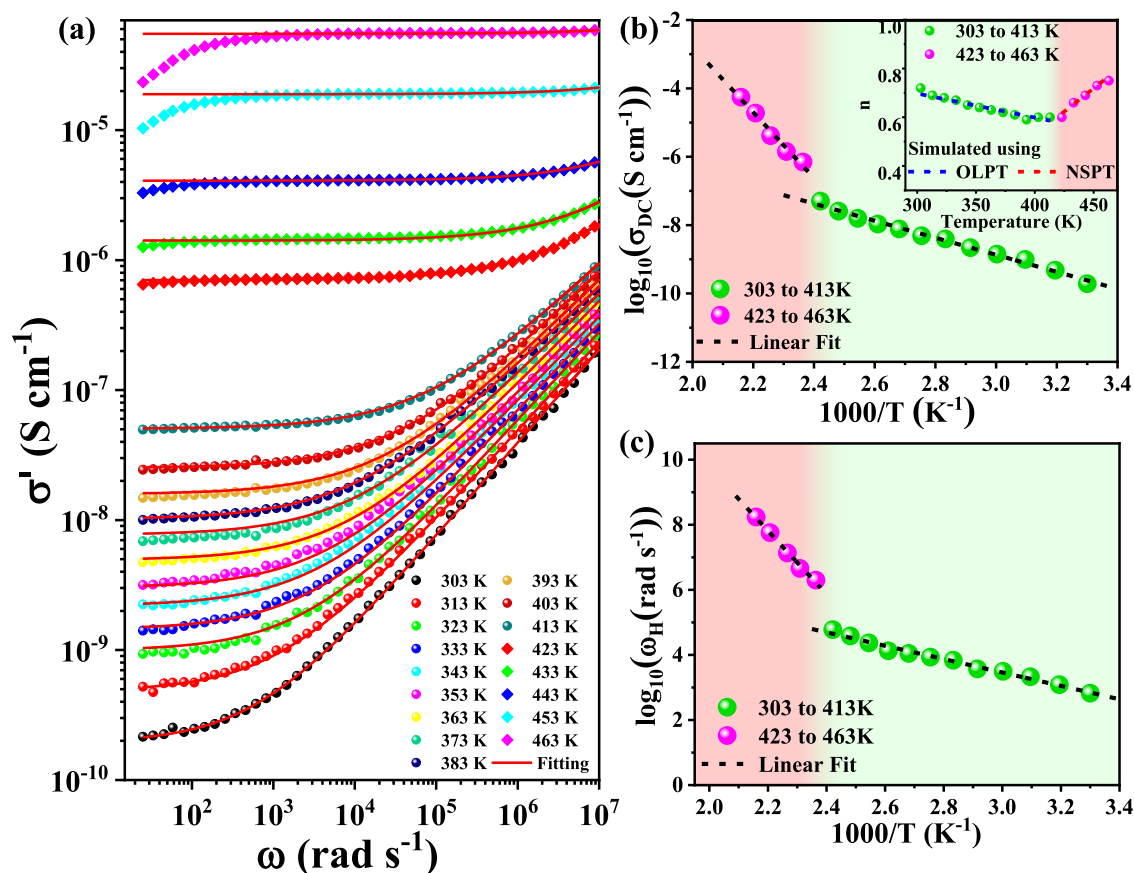FIG. 5. (a) Variation in the AC conductivity values with frequency at different temperatures. (b) σ_{dc} vs $1000/T$ plot; inset: frequency exponent n as a function of temperature. The dashed lines are fits corresponding to the OLPT in the low-temperature range and the NSPT in the high-temperature range, respectively. (c) ω_H vs $1000/T$ plot of $Cs_2PbI_2Cl_2$ showing Arrhenius-type behavior in two distinctly different temperature regions: the low-temperature region and the high-temperature regime shown in different shades. Linear fits are performed to obtain the activation energies associated with the two distinct temperature regimes. The onset of vacancy-mediated ionic transport mechanism is demonstrated beyond a temperature of 413 K.

where A represents a proportionality factor, ω signifies the applied angular frequency, and n is an exponent between 0 and 1. The CPE varies from being a perfect capacitance to an ideal resistance as the n value decreases from 1 to 0. Three parallel R-CPE circuits are connected in series in the equivalent circuit model corresponding to parameters associated with the contributions from grains, grain boundaries, and the sample-electrode interface [48,54]. It was noted that the grain-boundary resistance (R_{gb}) is higher than the grain resistance (R_g), particularly in the low-temperature region. Usually this is ascribed to the disordered arrangement of atoms near the grain boundary, which increases the electron scattering centers. We also note the decrease of the grain and grain boundary resistance values at higher temperatures, as shown in Fig. 4(e). This decrease in the resistance value indicates a reduction in the energy barrier, leading to a notable increase in the concentration of charges. Figure 4(f) displays the capacitance values of the grain (C_g), and grain boundary (C_{gb}) obtained from fitting the Nyquist plots at different temperatures. Since grain boundaries are more active in trapping charge carriers (consequently reducing their mobility), they show a more assertive capacitive behavior. The increase in the value of the capacitance with increasing temperature signifies

that more charges are now accumulated in the grains and grain boundaries.

C. Frequency-dependent AC conductivity

The frequency-dependent AC conductivity of the prepared sample was extensively studied to understand the ionic conduction mechanism for long-range and short-range dynamics of ions in $Cs_2PbI_2Cl_2$ RPHP. It has been established that the ions hop from one site to another throughout the lattice at low frequencies, resulting in long-range dynamics, but at high frequencies, the hopping motion of the ions is limited between the localized sites, resulting in short-range dynamics of ions [55]. Figure 5(a) depicts the variation in the AC conductivity as a function of applied frequency for different temperatures in the range of 313 to 463 K, increased in steps of 10 K. Notably, a distinct jump in the value of the AC conductivity occurs at 423 K. Additionally, the behavior of the AC conductivity can be categorized into two distinct regions: (1) the low-temperature region (LTR) spanning a temperature range of 303–413 K and (2) the high-temperature region (HTR) in the temperature range of 423–463 K. In the LTR, no appreciable changes are observed in the AC conductivity up to a

particular frequency (plateaus or frequency-independent regions), after which the conductivity increases as the frequency is increased. Typically, these plateaus correspond to DC conductivity (associated with long-range ion mobility) and are found to be prominent at relatively higher temperatures. The AC conductivity, on the other hand, does not have a substantial plateau region at low temperatures. At low frequencies, the activated hopping results in random diffusion of charge carriers, creating the DC conductivity (σ_{DC}), while in the dispersive region, ions move in a correlated forward-backward motion. This frequency-dependent and frequency-independent conductivity can be explained by the jump relaxation model (JRM) proposed by Funke *et al.* [56]. According to this model, after an ion hops out of its local configuration, it cannot be placed in equilibrium with its neighbors. The neighboring ions will reconfigure to ensure the most stable position of the ion. This is known as "successful hopping." However, the hopping is not always successful, and at times, after an initial hop, the ion finds itself in a nonequilibrium position with respect to its neighbors. So it jumps back to its original configuration after the first jump to achieve a partially relaxed arrangement, which is called "forward-backward jump" or "unsuccessful hopping." According to the model, the conductivity at low frequencies is mostly caused by a successful hop that is linked to the long-range translational motion of the ions. In the case of AC conductivity, more instances of unsuccessful hopping take place in the high-frequency region, and the motion of ions is dominated by forward-backward-forward jumps. The ratio of successful to unsuccessful hopping varies with frequency, which makes the conductivity spectra more dispersive. This is the normal ionic conduction mechanism in a dielectric material.

The frequency-independent regions (plateaus) shift towards the high-frequency domain with increasing temperature. The AC conductivity response in the HTR (423 to 463 K) can further be categorized into three distinct regions demonstrating (1) a low-frequency dispersion, (2) an intermediate frequency dispersion (flattened region or plateaus), and (3) a high-frequency dispersion. The low-frequency dispersion is ascribed to electrode polarization (EP) [57] and is characterized by lower conductivity due to ion blockage at the sample electrode interface. The EP is prevalent in the low-frequency part of the spectra, increasing with the rise in temperature and conductivity [58,59]. As the frequency increases slightly, the conductivity shows a flattened region attributed to long-range ionic motion, i.e., DC conductivity (σ_{DC}) and the conductivity for the rest of the region in the HTR spectra shows similar behavior as the LTR spectra. The switchover frequency from frequency-independent (DC conductivity) to the (high) frequency-dependent dispersive region is identified as the hopping frequency (ω_H). To quantitatively describe the ion conduction mechanism, the conductivity spectra were fitted using the modified Jonscher power law (also known as the Almond and West model) given by [60]

$$\sigma'(\omega) = \sigma_{DC}\left[1 + \left(\frac{\omega}{\omega_H}\right)^n\right]. \qquad (2)$$

Here σ_{DC} is the DC conductivity, ω_H is hopping frequency, and n is the power-law exponent representing the degree of interaction between ions and the lattices around them, whose

value lies within $0 < n \leqslant 1$. The solid lines in Fig. 5(a) represent the fitting excluding the regions of EP dominant in the HTR. The values of σ_{DC}, ω_H, and n obtained from the fits are tabulated in Table S1 [42]. We have plotted σ_{DC} vs $1000/T$ in Fig. 5(b), which obeys the Arrhenius relation with two distinct variations in slope corresponding to the LTR and HTR. The Arrhenius relation is given by

$$\sigma_{DC}(T) = \sigma_o \exp\left(\frac{-E_\sigma}{k_B T}\right). \qquad (3)$$

Here σ_0, E_σ, and k_B represent the pre-exponential factor, the activation energy, and the Boltzmann constant, respectively. The data were fitted with straight lines using the least-squares method separately in the LTR and HTR, and the activation energies ($E_{\sigma 1}$ and $E_{\sigma 2}$) obtained from the fits are ~ 0.48 (± 0.02) eV ($E_{\sigma 1}$) in the LTR and 1.82 (± 0.02) eV ($E_{\sigma 2}$) in the HTR.

The ω_H vs $1000/T$ plot shown in Fig. 5(c) also follows the Arrhenius relation and behaves similarly to Fig. 5(b):

$$\omega_H = \omega_0 \exp\left(-\frac{E_H}{k_B T}\right). \qquad (4)$$

The activation energies obtained from the reciprocal temperature dependence of the hopping frequency are ~ 0.48 (± 0.02) eV in the LTR and ~ 1.9 (± 0.02) eV in the HTR. It is observed that the activation energies obtained for both σ_{DC} and ω_H complementarily corroborate each other in the 2D $Cs_2PbI_2Cl_2$ RPHP. While the activation energy value at LTR suggests a normal ionic conduction and relaxation mechanism in the 2D $Cs_2PbI_2Cl_2$ RPHP, the high activation energy at HTR proposes the onset of a vacancy-mediated ionic transport mechanism with enhanced ionic conductivity as one progresses from the LTR to the HTR. We have also calculated the DC conductivity using

$$\sigma_{DC} = \frac{t}{RA}, \qquad (5)$$

where t is the distance between the two electrodes or thickness of the pellet, A is the mean area of the electrodes, and R ($R_g + R_{gb} + R_{ed}$) is the total resistance that we have obtained from fitting the Nyquist plots. After calculating the DC conductivity for all the temperatures, we have plotted σ_{DC} vs $1000/T$ in Fig. S8 [42]. It may be noted that the value of σ_{DC} obtained from power-law fits of the AC conductivity matches that obtained from the Nyquist plots. Even from this plot, the corresponding activation energies in the LTR and HTR regions are found to be ~ 0.53 (± 0.02) eV and ~ 1.87 (± 0.02) eV, respectively, which are very close to the obtained activation energies from the AC conductivity data.

It is noteworthy that the halide perovskites are mixed ionic and electronic conductors [61–63], but electrons form polarons due to lattice deformation present in the perovskites. This is indicated by the inset of Fig. 5(b), in which it is observed that the power-law exponent n changes with temperature. In the LTR, it initially decreases with temperature, reaches a minimum value, and increases slightly, whereas, in the HTR, it increases with temperature, which is an indication of different AC conduction mechanisms being prevalent in the LTR and HTR. Based on this temperature-dependent behavior of the power-law exponent (or frequency exponent n), it can

be said that in the LTR, the AC conduction mechanism follows the overlapping large polaron tunneling (OLPT) model, while in the HTR it follows the nonoverlapping small polaron tunneling model (NSPT) among the different theoretical models that invoke the contribution of different types of polarons to the AC conduction mechanism [64–67].

The polaron tunneling mechanism in the OLPT model deals with the cases when the polaron distortion clouds start to overlap. In the case of large polarons, the spatial area of the polaron is wider than the interatomic spacing, and the potential wells at adjacent sites may overlap. Consequently, the polaron hopping energy diminishes since the activation energy related to the motion of the charge carriers between the various sites decreases following [65,66]

$$W_H = W_{H0} \times \left(1 - \frac{r_p}{R}\right), \tag{6}$$

where r_p represents the radius of the large polaron and W_H refers to the polaron hopping energy.

W_{H0} is given by

$$W_{H0} = \frac{e^2}{4\varepsilon_p r_p}, \tag{7}$$

where ε_p is the effective dielectric constant. In the OLPT model, W_{H0} is expected to be a constant for all sites, while the intersite separation (R) is a variable.

The AC conductivity in the OLPT model is given by [65,66]

$$\sigma_{AC} = \frac{(\pi^2 e)^2 (k_B T)^2 \omega [N(E_F)]^2 R_\omega^4}{12\left(2\alpha k_B T + \frac{W_{H0} r_p}{R_\omega^2}\right)}, \tag{8}$$

where $N(E_F)$ is the density of states at the Fermi level and the tunneling distance (R_ω) at frequency ω is estimated as follows:

$$(R_\omega')^2 + [\beta W_{H0} + \ln(\omega \tau_0)]R_\omega' - \beta W_{H0} r_p' = 0 \tag{9}$$

with $R_\omega' = 2\alpha R_\omega$, $\beta = 1/k_B T$, $r_p' = 2\alpha r_p$, and α^{-1} denotes the spatial extension of the polaron wave function.

Thus in the OLPT model, n corresponds to the following equation:

$$n = 1 - \frac{8\alpha R_\omega + \frac{6W_{H0} r_p}{R_\omega k_B T}}{\left[2\alpha R_\omega + \frac{W_{H0} r_p}{R_\omega k_B T}\right]}. \tag{10}$$

Using the above equations (6)–(10), we have simulated the value of n, and the results are shown in the inset of Fig. 5(b) for the low-temperature range of 303–413 K. Table S2 [42] collates the values of different parameters obtained from the best fits to the equations. The theoretical calculations using the OLPT approach [Eq. (8)], which is used in the low-temperature region (Fig. S9 [42]), fit well with the experimental data. Table S3 [42] presents the parameter values at three different frequencies.

However, the OLPT model does not emulate the variation in n in the HTR. The AC conductivity at high temperatures is explained by the NSPT model, which considers the tunneling of carriers or polarons trapped at the structural defects. The cloud distortion of such polarons does not overlap. In the

NSPT model, the exponent n is calculated using [65]

$$n = 1 - \frac{4}{\ln\left(\frac{1}{\omega \tau_0}\right) - \frac{W_H}{k_B T}}. \tag{11}$$

The characteristic relaxation time τ_0 is around 10^{-13} s (the order of atomic vibrational period), and W_H represents the polaron hopping energy. We have simulated the value of n in the high-temperature region using Eq. (11) and plotted the same in the inset of Fig. 5(b).

Further, in the NSPT model, the AC conductivity is expressed as [66]

$$\sigma_{AC} = \frac{(\pi^2 e)^2 k_B T \alpha^{-1} [N(E_F)]^2 \omega R_\omega^4}{24}, \tag{12}$$

where

$$R_\omega = \frac{1}{2\alpha}\left[\ln\left(\frac{1}{\omega \tau_0}\right) - \frac{W_H}{k_B T}\right], \tag{13}$$

where R_ω represents the tunneling distance. We have fitted the AC conductivity (Fig. S9 [42]) for the HTR using Eqs. (12) and (13) considering the NSPT model, and the parameter values obtained from the best fits are enlisted in Table S4 [42].

In this investigation, two important phenomena have been observed: (a) the frequency-dependent AC conductivity curve shows a jump in the value of AC conductivity beyond 413 K, and (b) both the σ_{DC} vs $1000/T$ and ω_H vs $1000/T$ plots comprise two distinctly different regions (the LTR and the HTR) with different slopes in the Arrhenius plots leading to two different activation energies associated with two different ionic transport mechanisms. Plausible explanations of the two different slopes and jump in the ionic conductivity beyond a critical temperature separating the LTR and the HTR are as follows. At low temperatures, a lower value of the activation energy is sufficient to allow the migration of ions into the vacancies already present (e.g., Cl vacancy, such as in our case). As a result, a low number of ions participate in the conduction mechanism leading to low ionic conductivity. At high temperatures, the thermal energy available is sufficiently high to create vacancies, and the activation energy represents a combination of the energy required for vacancy generation and the motion of ions into the vacancy. Here this vacancy-assisted anion conduction is in addition to the cationic and anionic conductions that are already present. As a result, we observe a large value of the DC conductivity. A large number of ions are now available to participate in ionic conduction resulting in a jump in the value of the ionic conductivity. This results in the onset of vacancy-mediated ionic conduction characterized by a large value of the activation energy [68,69].

D. Study of complex dielectric permittivity

The variation of the dielectric constant as a function of applied frequency has been investigated in the temperature range of 303–463 K. The complex dielectric spectroscopy of a material can be represented as

$$\varepsilon^*(\omega) = \varepsilon'(\omega) - j\varepsilon''(\omega). \tag{14}$$

Here $\varepsilon'(\omega)$ is the real part of complex dielectric permittivity $\varepsilon^*(\omega)$ and represents the stored energy. In contrast, $\varepsilon''(\omega)$ is the imaginary part of the dielectric constant that represents the energy dissipation or loss factor associated with the process of polarization. $\varepsilon'(\omega)$ and $\varepsilon''(\omega)$ can be calculated from the measured impedance spectra using the following equations:

$$\varepsilon'(\omega) = \frac{Z'}{\omega C_0(Z'^2 + Z''^2)}, \tag{15}$$

$$\varepsilon''(\omega) = \frac{Z''}{\omega C_0(Z'^2 + Z''^2)}. \tag{16}$$

Here $C_0(= \varepsilon_0 A/d)$ is the free space capacitance, ε_0 is the permittivity of free space, A is the area of the electrode, and d is the thickness of the pellet. The dielectric constant plays an extensive role in the various ionic conduction processes, primarily governed by the four polarization types, namely, ionic, electronic, orientational, and interfacial.

Figures 6(a) and 6(b) represent the frequency dependence of the real part $\varepsilon'(\omega)$ (dielectric constant) and the imaginary part $\varepsilon''(\omega)$ (dielectric loss) of complex dielectric spectra in the temperature range 313–463 K, respectively. The value of dielectric constant $\varepsilon'(\omega)$ and dielectric loss $\varepsilon''(\omega)$ shown in Figs. 6(a) and 6(b), respectively, is higher in the low-frequency region, and it starts to decrease gradually as the frequency increases and become almost temperature and frequency independent in the high-frequency region. Similar to the other dielectric parameters, a leap in the values of $\varepsilon'(\omega)$ and $\varepsilon''(\omega)$ is observed in Figs. 6(a) and 6(b) beyond 413 K, which segregates the data in the LTR and HTR. The dielectric constant $\varepsilon'(\omega)$ and dielectric loss $\varepsilon''(\omega)$ play a crucial role in the field of ionic conduction process governed by polarization. The electronic and ionic polarizations behave as deformational components, while the interfacial and orientation polarizations seem to be the relaxation components of the polarization [70]. The change of $\varepsilon'(\omega)$ with frequency can be elucidated by the Maxwell-Wagner interfacial polarization, which merges with Koops's phenomenological theory [50,71]. According to this hypothesis, interfacial polarization is essential in the low-frequency domain because of the appearance of double layers in dielectric materials. According to the theory, dielectric materials are likewise approximated to be constituted of low-resistive layers of grains. The barriers that separate these grains have a moderately low conductivity. Charge carriers are trapped at the grain boundary interface, preventing them from moving freely [72]. Interfacial polarization involves electron exchange between the ions of the same molecule. The material deformation causes the altering distribution of positive and negative space charges.

When an electric field is applied, negative and positive charges migrate to opposing poles, resulting in a huge number of dipoles. At low frequencies ($\omega \ll 1/\tau$), the dipoles quickly follow the quasistatic field, and the material has a high dielectric constant at low frequencies. As the dipole moments become incapable of following the electric field at higher frequencies, the dielectric constants gradually fall into the high-frequency zone. Therefore, the orientational and interfacial polarizations contribute to the real part of the dielectric constant in the low-frequency zone. In contrast, the electronic
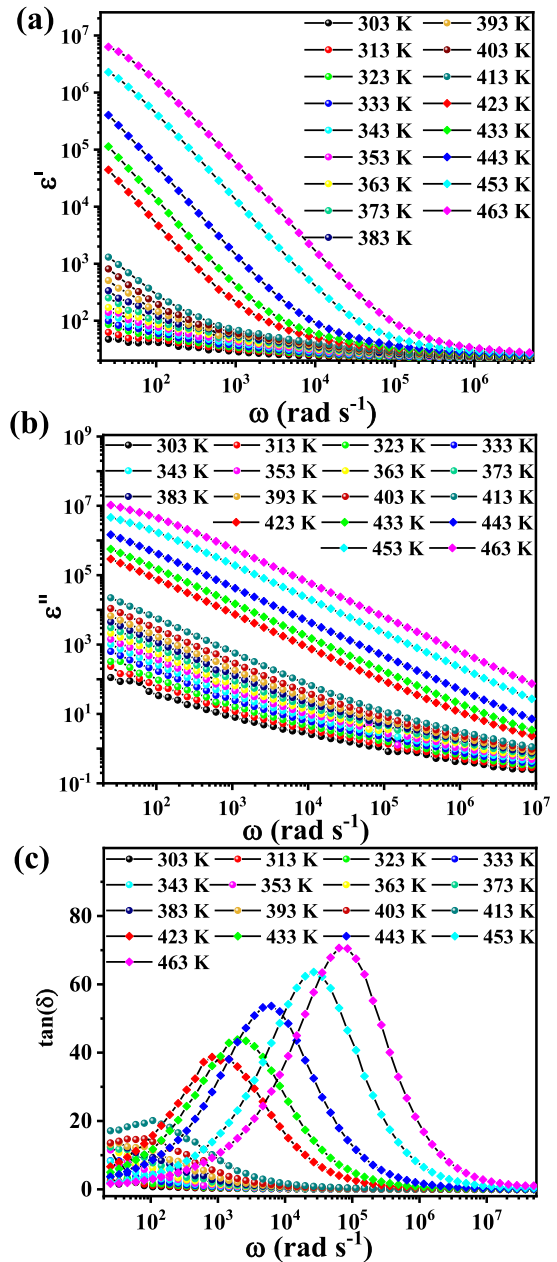

FIG. 6. Frequency dependence of (a) dielectric constant (ε'), (b) dielectric loss (ε''), and (c) loss tangent ($\tan\delta$) at different temperatures for the 2D $Cs_2PbI_2Cl_2$ RPHP.

and ionic polarizations are predominant in the high-frequency domain, which explains the lower values of $\varepsilon'(\omega)$. Furthermore, for a particular frequency, the values of $\varepsilon'(\omega)$ increase with the increase in temperature. This behavior is indicative of the presence of thermally activated charge carriers, which impact the polarization.

The dielectric loss $\varepsilon''(\omega)$ also decreases with frequency for a specific temperature. According to Koop's theory, any impurity or imperfection in a material can form a potential barrier to transporting the charge carriers. The partial conduction of charges is restricted by space charge polarization until they clog at a potential barrier or grain boundary. As a result of the grain boundary dominance in the low-frequency
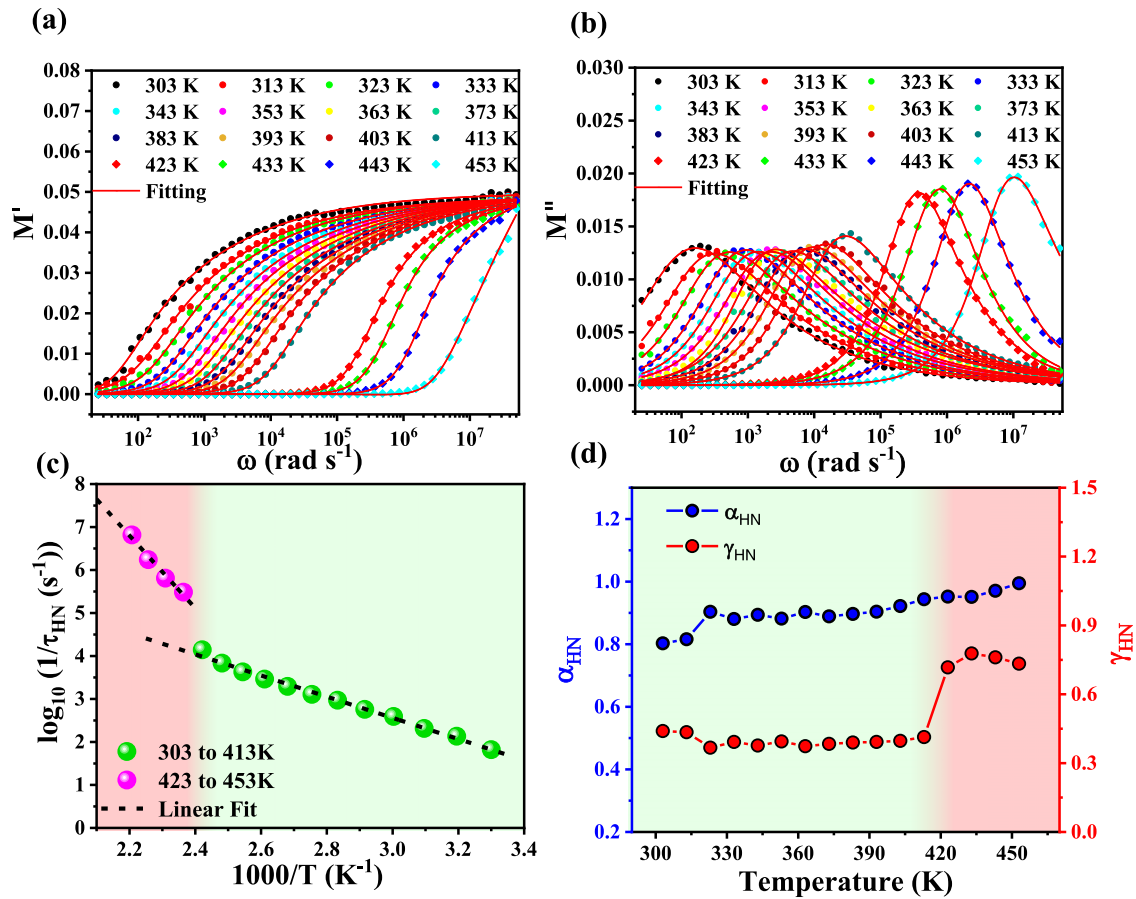
FIG. 7. Variation of (a) real $M'(\omega)$ and (b) imaginary $M''(\omega)$ parts of complex electric modulus with frequency. (c) The relaxation time and reciprocal of the sample temperature showing Arrhenius-type behavior with two different slopes corresponding to the LTR and the HTR. (d) Variation of α_{HN} and γ_{HN} for the Cs$_2$PbI$_2$Cl$_2$ RPHP at different temperatures.

band, electrons require more energy to hop, resulting in an increased dielectric loss. On the other hand, when frequency increases, the low-resistive grains become prominent, and hopping electrons are unable to follow the applied electric field. As a result, the exchange of electrons between the ions of the same compound requires very little energy, resulting in a reduction in the dielectric loss in the high-frequency zone. In the low-frequency zone, four types of polarizations are present; however, only ionic and electronic polarization play a significant role in the high-frequency region, resulting in a decrease in the dielectric loss factor in the high-frequency region for the temperature range (303–463 K) [73,74]. The value of dielectric loss increases with the rise in temperature because the presence of thermally activated charge carriers is accountable for such enhancement.

In addition, we have investigated the loss tangent (tan δ), which provides information about the energy loss due to the conduction of the charge carriers. The loss tangent can be expressed as the ratio of dielectric loss to dielectric constant, tan $\delta = \varepsilon''/\varepsilon'$. The frequency dependence of loss tangent spectra at different temperatures is shown in Fig. 6(c). Here the value of the loss tangent diminishes when the frequency increases beyond the relaxation frequency and reaches a constant value at a high frequency. The dominant nature of dipolar polarization may explain the appearance of peaks in the low-frequency range. With an increase in temperature, the

values of the loss tangent increase, and the peaks move correspondingly, confirming that dipolar polarization is a thermally controlled mechanism. The complete loss spectrum with relaxation frequency is observed in HTR. This loss tangent peak appears when the hopping frequency matches the frequency of the applied AC field. This hopping process suggests that a large amount of thermally activated charge carriers produce a large conductivity, which we have already observed in our conductivity spectra [75].

E. Complex electric modulus spectra

We have further investigated the relaxation mechanism in the 2D Cs$_2$PbI$_2$Cl$_2$ RPHP by analyzing the complex electric modulus spectra (CEMS). It is represented as $M^*(\omega)$, which is associated with the complex dielectric permittivity $\varepsilon^*(\omega)$ by a relation [76]

$$M^*(\omega) = \frac{1}{\varepsilon^*(\omega)} = \frac{1}{\varepsilon' - j\varepsilon''} = \frac{\varepsilon'}{\varepsilon'^2 + \varepsilon''^2} + j\frac{\varepsilon''}{\varepsilon'^2 + \varepsilon''^2}$$
$$= M'(\omega) + jM''(\omega), \qquad (17)$$

where $M'(\omega)$ and $M''(\omega)$ are real and imaginary parts of complex electric modulus $M^*(\omega)$, respectively. Figures 7(a) and 7(b) represent the variation of $M'(\omega)$ and $M''(\omega)$ as a function of frequency in the temperature range from 303 to 453 K, respectively. In Fig. 7(a) the value of $M'(\omega)$ is very low

at low frequencies for all temperatures, gradually increasing with frequency and showing a plateau-like behavior at high frequencies. In the HTR (beyond 413 K), the value of $M'(\omega)$ is initially very low and remains constant up to a specific high-frequency value beyond which the $M'(\omega)$ starts increasing on further increments in the frequency. This behavior is attributed to long-range charge carrier mobility [50].

The $M''(\omega)$ spectra show distinct, significant peaks for all temperatures, which can be ascribed to the relaxation frequency of the material. The long-range motions of ions are represented by the left side (low-frequency region), while the localized motions of ions are represented by the right side (high-frequency region), of each peak in the $M''(\omega)$ curve. This is indicative of a transition from long-range to short-range mobility of ions with an increase in the frequency. The rapid movement of ions causes a continuous shift in the $M''(\omega)$ peak towards the higher frequency region with increasing temperature. This signifies that the relaxation time (corresponding to the frequency of the peak in the spectra) decreases with increasing temperature, indicating thermally induced relaxation behavior in the 2D $Cs_2PbI_2Cl_2$ RPHP. The asymmetric nature of the relaxation peaks suggests that the relaxation mechanism in the prepared material is non-Debye type. Further insight into the asymmetric nature of peaks is provided by the analysis of the CEMS (M' and M'') using the HN model expressed as [77]

$$M^*(\omega) = M_\infty + \left(\frac{M_s - M_\infty}{[1 + (j\omega\tau_{HN})^{\alpha_{HN}}]^{\gamma_{HN}}} \right), \quad (18)$$

where M_s and M_∞ are the low- and high-frequency limiting values, respectively, of the $M'(\omega)$, τ_{HN} is the relaxation time, and α_{HN} and γ_{HN} are the shape parameters with limiting conditions $0 < \alpha_{HN}(\text{or } \gamma_{HN}) \leqslant 1$ and $0 < (\alpha_{HN}\gamma_{HN}) \leqslant 1$. The CEMS of $Cs_2PbI_2Cl_2$ RPHP at different temperatures are fitted to the real and imaginary parts of Eq. (18) and shown alongside the plots in Figs. 7(a) and 7(b), respectively. Figure 7(c) shows the plot of relaxation time τ_{HN}, obtained from the best fits, as a function of the reciprocal temperature, which obeys Arrhenius behavior,

$$\tau_{HN} = \tau_0 \exp\left(\frac{E_{HN}}{k_B T} \right). \quad (19)$$

The clear segregation of this plot into two separate regions corresponding to the LTR and HTR is observed, similar to the DC conductivity and hopping frequency plots as a function of the reciprocal temperature. The activation energy calculated from the linear fits in the LTR (303–413 K) is $E_{HN1} \sim 0.46 \ (\pm 0.02)$ eV, whereas that in the HTR (423–453 K) is $E_{HN2} \sim 1.86 \ (\pm 0.02)$ eV, which are close to the activation energies $E_{\sigma 1}$ and $E_{\sigma 2}$ estimated from the DC conductivity plot. Figure 7(d) shows the variation in the shape parameters α_{HN} and γ_{HN} as a function of temperature obtained from the best fits of the CEMS in the $Cs_2PbI_2Cl_2$ RPHP. The corresponding values of α_{HN} and γ_{HN} are shown in Table S5 [42]. The values of α_{HN} do not show any appreciable change with temperature, whereas the values of γ_{HN} increase slowly with the increase in temperature and exhibit a sudden jump beyond 413 K. The jump in γ_{HN} signifies the increase in the peak asymmetry of M'' at HTR [78]. The CEMS has also been analyzed using the

Kohlrausch-Williams-Watts (KWW) formalism given by [79]

$$M^*(\omega) = M_\infty \left[1 - \int_0^\infty \left(-\frac{d\phi}{dt} \right) e^{-j\omega t} \, dt \right], \quad (20)$$

where the relaxation function $\phi(t)$ describes the decay of the applied electric field $E(t)$ in the time domain. In the KWW formalism, the relaxation function $\phi(t)$ can be expressed as

$$\phi(t) = \exp\left[-\left(\frac{t}{\tau_{KWW}} \right)^\beta \right], \quad (21)$$

where τ_{KWW} is the KWW relaxation time and $\beta \ (0 < \beta \leqslant 1)$ is the stretched exponent [80]. The relaxation function $\phi(t)$ is calculated from the inverse Fourier transform of Eq. (20) given by [81]

$$\phi(t) = \frac{2}{\pi} \int_0^\infty \frac{M''}{\omega M_\infty} \cos(\omega t) d\omega. \quad (22)$$

Figure 8(a) shows the relaxation function $\phi(t)$ derived from the best fit of Eq. (22) to the modulus data for the 2D $Cs_2PbI_2Cl_2$ RPHP at various temperatures. Parameters evaluated from the fitting of complex modulus spectra using KWW model are shown in Table S6 [42]. Figure 8(b) shows the inverse KWW relaxation time $(1/\tau_{KWW})$ as a function of the reciprocal temperature, which also follows the Arrhenius behavior [75]. This Arrhenius relation can also be segregated into two distinct temperature regions and gives the activation energy of $\sim 0.48 \ (\pm 0.02)$ eV in the LTR and $\sim 1.89 \ (\pm 0.02)$ eV in the HTR. The temperature variation of the stretched exponent β obtained from the above fits using KWW and HN relaxation $\beta_{HN} = (\alpha_{HN}\gamma_{HN})^{\frac{1}{1.23}}$ is shown in Fig. 8(c) [21]. The low value of β in the low-temperature region (LTR) represents the cooperative motion of the mobile ions [80]. These values of β at LTR lead to the dynamics of ions as the mobile ions jump from one site to another. In the high-temperature region (beyond 413 K), there is an abrupt jump in the β value, which now exhibits a high-value representative of the fact that the dynamics of the ions have now changed from normal ionic conduction to vacancy-mediated ionic conduction.

F. Scaling of conductivity and electric modulus spectra

Scaling is an important feature in any case of data interpretation. The study of the conductivity spectra at different temperatures of various materials leads to a scaling law, which shows a time-temperature superposition [82–86]. Scaling different data together to form a single common curve suggests that the process can be distinguished as a physical mechanism modified only by thermodynamic scales [85]. The scaling behavior has been studied by many researchers using various parameters and formalisms [82–86]. Here we have performed the scaling behavior of temperature-dependent conductivity and CEMS in $Cs_2PbI_2Cl_2$ RPHP, as shown in Fig. 9. In the case of conductivity scaling, we have plotted (σ'/σ_{DC}) vs $\log(\omega/\sigma_{DC}T)$ at different temperatures for 2D $Cs_2PbI_2Cl_2$ RPHP [as shown in Fig. 9(a)]. The inset of Fig. 9(a) clearly shows two master curves at the two regions LTR and HTR, so it illustrates different dynamic processes occurring at LTR and HTR characterized by two different activation energies. The scaling curve of the electric modulus for this 2D $Cs_2PbI_2Cl_2$
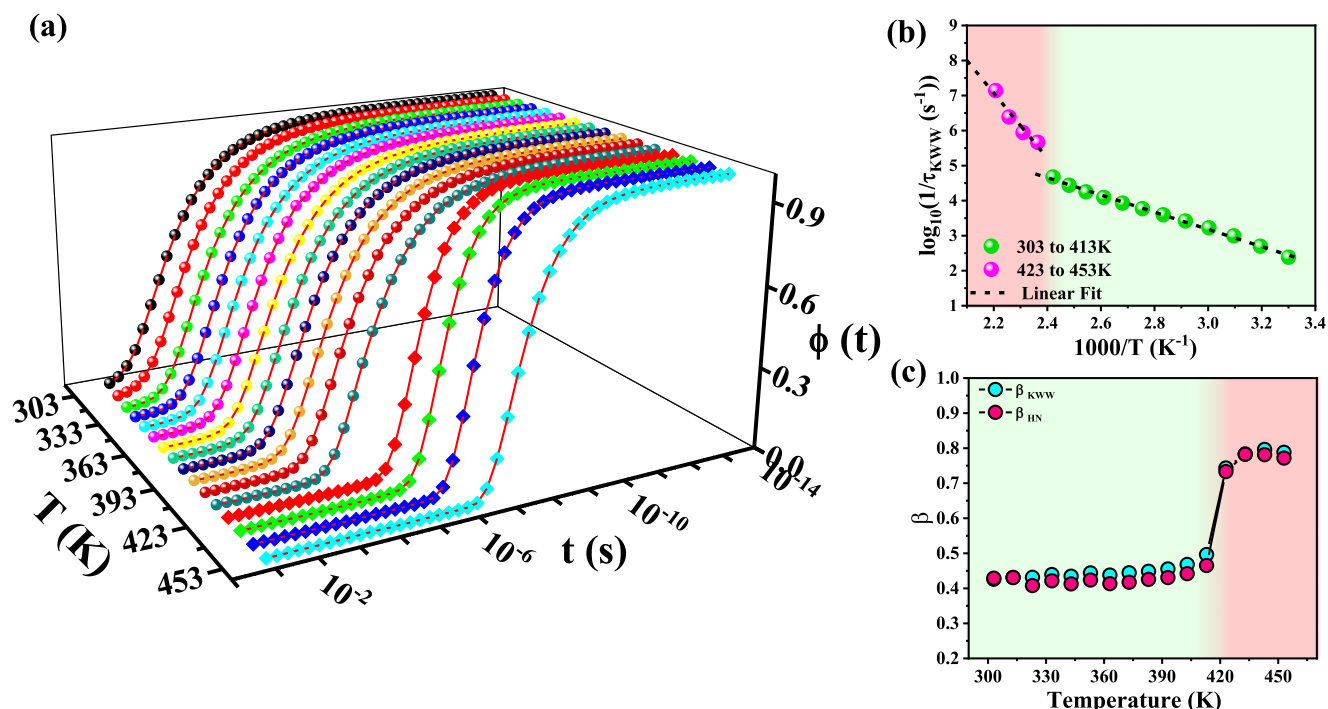
FIG. 8. (a) Plot of time and temperature dependence of $\phi(t)$. (b) $(1000/T)$ dependence of the reciprocal KWW relaxation time $(1/\tau_{KWW})$ showing Arrhenius-type behavior with dashed lines representing the straight-line fits, and (c) variation in β values, obtained independently from the KWW and HN relaxation mechanisms, as a function of temperature for $Cs_2PbI_2Cl_2$ RPHP.

is shown in Fig. 9(b), in which the relaxation frequency ω_{max} scales each frequency and $M''_{max}(\omega)$ scales $M''(\omega)$. All the scaled modulus spectra for different temperatures overlap into two master curves; one is for LTR, and another is for the HTR region, indicating the two different dynamical processes in the 2D $Cs_2PbI_2Cl_2$ RPHP sample. Here the LTR demonstrates a normal ionic conduction mechanism, whereas the HTR shows vacancy-mediated ionic conduction.

V. CONCLUSIONS

A 2D layered Ruddlesden-Popper (RP) halide perovskite is synthesized using a simple mechanochemical method. The ionic conduction and dielectric relaxation have been probed using dielectric spectroscopic measurements over a wide temperature and frequency range. By analyzing the dielectric attributes from complex impedance spectroscopy, AC conductivity, and complex electric modulus using the
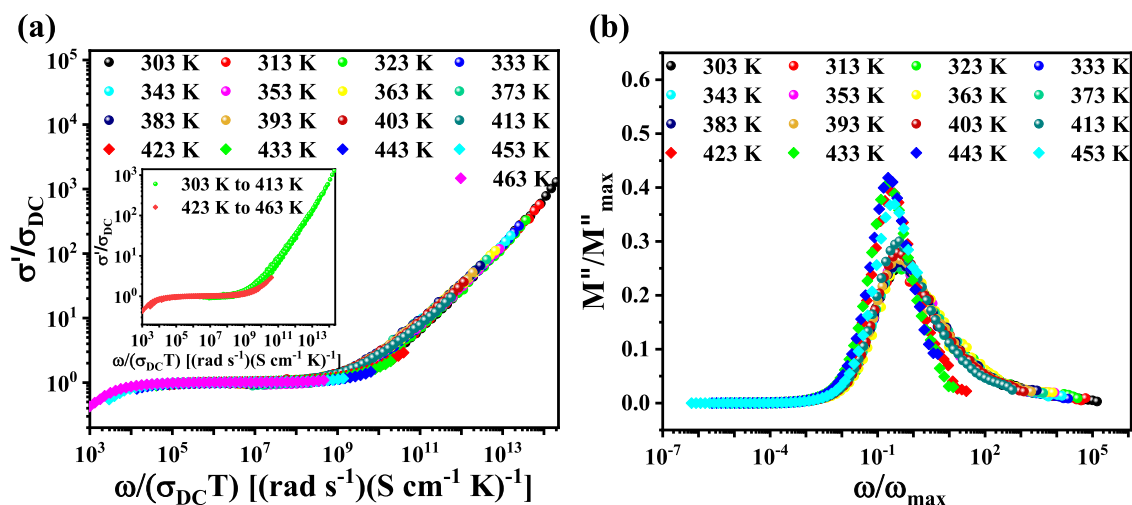

FIG. 9. (a) Scaling of the AC conductivity spectra $\sigma'(\omega)$ at different temperatures for $Cs_2PbI_2Cl_2$ RPHP. The inset shows the two distinct scaling curves corresponding to the LTR and the HTR. (b) The electric modulus loss $M''(\omega)$ also demonstrates two distinct scaling curves (one each corresponding to the LTR and the HTR) for the $Cs_2PbI_2Cl_2$ RPHP at different temperatures.

Maxwell-Wagner equivalent circuit model, universal power law, Havrilliak-Negami model, and Kohlrausch-Williams-Watts model, fundamental aspects of the ionic transport and relaxation mechanism in 2D layered RP perovskite are investigated. The Nyquist plots indicate the grain and grain boundary contributions to the total impedance. In temperature-dependent AC conductivity spectra, there is a critical temperature beyond which the conductivity increases abruptly. The temperature dependence of the AC conductivity and its power-law exponent was interpreted in terms of polaron tunneling models. The Arrhenius plot of the ionic conductivity above the critical temperature in the HTR yields substantially high activation energy $\sim 1.82 \, (\pm 0.02)$ eV due to anionic vacancy leading to large ionic conductivity (423–463 K). The activation energy calculated from the Arrhenius plot is $\sim 0.48 \, (\pm 0.02)$ eV in the LTR (303–413 K). The activation energies derived using the HN and KWW models are comparable with the activation energy calculated using the DC conductivity results. The validity of the time-temperature superposition principle is specified by the scaling of the AC conductivity and the modulus loss spectra at two different temperature regions: 303–413 K and 423–463 K. An abrupt change in all the measurements of dielectric spectra has been observed beyond a temperature 413 K, evidencing the onset of vacancy mediated ionic transport mechanism, which requires high activation energy and leads to high ionic conductivity in 2D layered RP perovskite.

[1] A. Kojima, K. Teshima, Y. Shirai, and T. Miyasaka, Organometal halide perovskites as visible-light sensitizers for photovoltaic cells, J. Am. Chem. Soc. **131**, 6050 (2009).

[2] M. Grätzel, The light and shade of perovskite solar cells, Nat. Mater. **13**, 838 (2014).

[3] C. Ahläng, M. Nyman, and R. Österbacka, Influence of the Electric Potential on Charge Extraction and Interface Recombination in Perovskite Solar Cells, Phys. Rev. Appl. **16**, 014041 (2021).

[4] S. Zeder, B. Ruhstaller, and U. Aeberhard, Assessment of Photon Recycling in Perovskite Solar Cells by Fully Coupled Optoelectronic Simulation, Phys. Rev. Appl. **17**, 014023 (2022).

[5] Y. Rong, Y. Hu, A. Mei, H. Tan, M. I. Saidaminov, S. I. Seok, M. D. McGehee, E. H. Sargent, and H. Han, Challenges for commercializing perovskite solar cells, Science **361**, eaat8235 (2018).

[6] Z. Huang, A. H. Proppe, H. Tan, M. I. Saidaminov, F. Tan, A. Mei, C. S. Tan, M. Wei, Y. Hou, H. Han, and S. O. Kelley, Suppressed ion migration in reduced-dimensional perovskites improves operating stability, ACS Energy Lett. **4**, 1521 (2019).

[7] H. J. Snaith and P. Hacke, Enabling reliability assessments of pre-commercial perovskite photovoltaics with lessons learned from industrial standards, Nature Energy **3**, 459 (2018).

[8] N. G. Park, M. Grätzel, T. Miyasaka, K. Zhu, and K. Emery, Towards stable and commercially available perovskite solar cells, Nature Energy **1**, 16152 (2016).

[9] L. Mao, C. C. Stoumpos, and M. G. Kanatzidis, Two-dimensional hybrid halide perovskites: Principles and promises, J. Am. Chem. Soc. **141**, 1171 (2019).

[10] Y. Chen, Y. Sun, J. Peng, J. Tang, K. Zheng, and Z. Liang, 2D Ruddlesden–Popper perovskites for optoelectronics, Adv. Mater. **30**, 1703487 (2017).

[11] H. Tsai, W. Nie, J. C. Blancon, C. C. Stoumpos, R. Asadpour, B. Harutyunyan, A. J. Neukirch, R. Verduzco, J. J. Crochet, S. Tretiak, and L. Pedesseau, High-efficiency two-dimensional Ruddlesden–Popper perovskite solar cells, Nature (London) **536**, 312 (2016).

[12] Y. Gao, Z. Wei, S. N. Hsu, B. W. Boudouris, and L. Dou, 2020. Two-dimensional halide perovskites featuring semiconducting organic building blocks, Mater. Chem. Front. **4**, 3400 (2020).

[13] C. Katan, N. Mercier, and J. Even, Quantum and dielectric confinement effects in lower-dimensional hybrid perovskite semiconductors, Chem. Rev. **119**, 3140 (2019).

[14] A. K. Jena, A. Kulkarni, and T. Miyasaka, Halide perovskite photovoltaics: Background, status, and future prospects, Chem. Rev. **119**, 3036 (2019).

[15] R. Chakraborty, G. Paul, and A. J. Pal, Dynamic response of alternating-current-driven light-emitting diodes based on hybrid halide perovskites, Phys. Rev. Appl. **14**, 024006 (2020).

[16] W. H. Guo, J. J. Shi, Y. H. Zhu, M. Wu, J. Du, Y. L. Cen, S. M. Liu, and S. P. Han, Two-Dimensional 111-Type In-Based Halide Perovskite $Cs_3In_2X_9$ ($X = $ Cl, Br, I) with Optimal Band Gap for Photovoltaics and Defect-Insensitive Blue Emission, Phys. Rev. Appl. **13**, 024031 (2020).

[17] T. Li, X. Zhao, D. Yang, M. H. Du, and L. Zhang, Intrinsic Defect Properties in Halide Double Perovskites for Optoelectronic Applications, Phys. Rev. Appl. **10**, 041001(R) (2018).

[18] J. Li, Q. Yu, Y. He, C. C. Stoumpos, G. Niu, G. G. Trimarchi, H. Guo, G. Dong, D. Wang, L. Wang, and M. G. Kanatzidis, $Cs_2PbI_2Cl_2$, all-inorganic two-dimensional Ruddlesden–Popper mixed halide perovskite with optoelectronic response, J. Am. Chem. Soc. **140**, 11085 (2018).

[19] S. Guo, K. Bu, J. Li, Q. Hu, H. Luo, Y. He, Y. Wu, D. Zhang, Y. Zhao, and W. Yang, Enhanced photocurrent of all-inorganic two-dimensional perovskite $Cs_2PbI_2Cl_2$ via pressure-regulated excitonic features, J. Am. Chem. Soc. **143**, 2545 (2021).

[20] P. Acharyya, T. Ghosh, K. Pal, K. Kundu, K. Singh, R. J. Pandey, A. Soni, and U. V. Waghmare, Intrinsically ultralow thermal conductivity in Ruddlesden–Popper 2D perovskite $Cs_2PbI_2Cl_2$: Localized anharmonic vibrations and dynamic octahedral distortions, J. Am. Chem. Soc. **142**, 15595 (2020).

[21] P. Pal and A. Ghosh, Broadband dielectric spectroscopy of BMPTFSI ionic liquid doped solid-state polymer electrolytes: Coupled ion transport and dielectric relaxation mechanism, J. Appl. Phys. **128**, 084104 (2020).

[22] S. Mandal and A. Ghosh, Electrical conduction in lead-iron glasses, J. Phys.: Condens. Matter **8**, 829 (1996).

[23] B. B. Zhang, F. Wang, H. Zhang, B. Xiao, Q. Sun, J. Guo, A. B. Hafsia, A. Shao, Y. Xu, and J. Zhou, Defect proliferation in $CsPbBr_3$ crystal induced by ion migration, Appl. Phys. Lett. **116**, 063505 (2020).

[24] A. Rivera, J. Santamaría, C. León, T. Blochowicz, C. Gainaru, and E. A. Rössler, Temperature dependence of the ionic conductivity in $Li_{3x}La_{2/3-x}TiO_3$: Arrhenius versus non-Arrhenius, Appl. Phys. Lett. **82**, 2425 (2003).

[25] T. Paul, P. K. Sarkar, S. Maiti, and K. K. Chattopadhyay, Multilevel programming and light-assisted resistive switching in a halide-tunable all-inorganic perovskite cube for flexible memory devices, ACS Appl. Electron. Mater. **2**, 3667 (2020).

[26] T. Paul, S. Maiti, N. Besra, B. K. Chatterjee, B. K. Das, S. Thakur, S. Sarkar, N. Das, and K. K. Chattopadhyay, Tailored $CsPbX_3$ nanorods for electron-emission nanodevices, ACS Appl. Nano Mater. **2**, 5942 (2019).

[27] P. Pal and A. Ghosh, Three-Dimensional $CsPbCl_3$ Perovskite Anode for Quasi-Solid-State Li-Ion and Dual-Ion Batteries: Mechanism of Li^+ Conversion Process in Perovskite, Phys. Rev. Appl. **14**, 064010 (2020).

[28] S. Mondal, T. Paul, S. Maiti, B. K. Das, and K. K. Chattopadhyay, Human motion interactive mechanical energy harvester based on all inorganic perovskite-PVDF, Nano Energy **74**, 104870 (2020).

[29] M. M. Lee, J. Teuscher, T. Miyasaka, T. N. Murakami, and H. J. Snaith, Efficient hybrid solar cells based on meso-superstructured organometal halide perovskites, Science **338**, 643 (2012).

[30] T. Paul, S. Maiti, B. K. Chatterjee, P. Bairi, B. K. Das, S. Thakur, and K. K. Chattopadhyay, Electrochemical performance of 3D network $CsPbBr_3$ perovskite anodes for Li-ion batteries: Experimental venture with theoretical expedition, J. Phys. Chem. C **125**, 16892 (2021).

[31] A. Sahoo, T. Paul, S. Maiti, and R. Banerjee, Temperature-dependent dielectric properties of $CsPb_2Br_5$: A 2D inorganic halide perovskite, Nanotechnology **33**, 195703 (2022).

[32] S. Ahmad, C. George, D. J. Beesley, J. J. Baumberg, and M. De Volder, Photo-rechargeable organo-halide perovskite batteries, Nano Lett. **18**, 1856 (2018).

[33] M. B. Bechir and M. H. Dhaou, Study of charge transfer mechanism and dielectric relaxation of $CsCuCl_3$ perovskite nanoparticles, Mater. Res. Bull. **144**, 111473 (2021).

[34] P. Maji, A. Ray, P. Sadhukhan, S. Chatterjee, and S. Das, Study on charge transfer mechanism and dielectric relaxation of cesium lead bromide ($CsPbBr_3$), J. Appl. Phys. **124**, 124102 (2018).

[35] S. Zhao and L. Xiao, Ion migration mechanism in all-inorganic Ruddlesden–Popper lead halide perovskites by first-principles calculations, Phys. Chem. Chem. Phys. **24**, 403 (2022).

[36] A. Karmakar, M. S. Dodd, X. Zhang, M. S. Oakley, M. Klobukowski, and V. K. Michaelis, Mechanochemical synthesis of 0D and 3D cesium lead mixed halide perovskites, Chem. Commun. **55**, 5079 (2019).

[37] D. Prochowicz, M. Franckevičius, A. M. Cieślak, S. M. Zakeeruddin, M. Grätzel, and J. Lewiński, Mechanosynthesis of the hybrid perovskite $CH_3NH_3PbI_3$: Characterization and the corresponding solar cell efficiency, J. Mater. Chem. A **3**, 20772 (2015).

[38] A. Karmakar, A. M. Askar, G. M. Bernard, V. V. Terskikh, M. Ha, S. Patel, K. Shankar, and V. K. Michaelis, Mechanochemical synthesis of methylammonium lead mixed–halide perovskites: Unraveling the solid-solution behavior using solid-state NMR, Chem. Mater. **30**, 2309 (2018).

[39] A. M. Askar, A. Karmakar, G. M. Bernard, M. Ha, V. V. Terskikh, B. D. Wiltshire, S. Patel, J. Fleet, K. Shankar, and V. K. Michaelis, Composition-tunable formamidinium lead mixed halide perovskites via solvent-free mechanochemical synthesis: Decoding the Pb environments using solid-state NMR spectroscopy, J. Phys. Chem. Lett. **9**, 2671 (2018).

[40] D. J. Kubicki, D. Prochowicz, A. Hofstetter, S. M. Zakeeruddin, M. Grätzel, and L. Emsley, Phase segregation in Cs-, Rb-and K-doped mixed-cation $(MA)_x(FA)_{1-x}PbI_3$ hybrid perovskites from solid-state NMR, J. Am. Chem. Soc. **139**, 14173 (2017).

[41] S. L. James, C. J. Adams, C. Bolm, D. Braga, P. Collier, T. Friščić, F. Grepioni, K. D. Harris, G. Hyett, W. Jones, and A. Krebs, Mechanochemistry: Opportunities for new and cleaner synthesis, Chem. Soc. Rev. **41**, 413 (2012).

[42] See Supplemental Material at http://link.aps.org/supplemental/10.1103/PhysRevMaterials.6.115002 for mechanochemical synthesis, detailed material characterization, reciprocal temperature dependence of σ_{DC} obtained from the complex impedance plots, variation of AC conductivity with respect to temperature at 10 kHz, 100 kHz, and 1 MHz, parameters estimated from fitting the AC conductivity data, parameter values obtained from fitting the power-law exponent (n) using the OLPT model and NSPT model, and parameters evaluated from the fitting of complex modulus spectra using the Havriliak-Negami (HN) model and Kohlrausch-Williams-Watts (KWW) model of $Cs_2PbI_2Cl_2$ RPHP.

[43] R. E. Patru, H. Khassaf, I. Pasuk, M. Botea, L. Trupina, C.-P. Ganea, L. Pintilie, and I. Pintilie, Tetragonal–cubic phase transition and low-field dielectric properties of $CH_3NH_3PbI_3$ crystals, Materials **14**, 4215 (2021).

[44] L. Cai and C. Feng, Effect of vacancy defects on the electronic structure and optical properties of GaN, J. Nanotechnol. **2017**, 6987430 (2017).

[45] S. Mishra, A. Sahoo, S. Mondal, P. Mandal, C. K. Ghosh, and D. Bhattacharya, Electric-field-driven resistive transition in multiferroic $SrCo_2Fe_{16}O_{27}/Sr_3Co_2Fe_{24}O_{41}$ composite, J. Appl. Phys. **131**, 204101 (2022).

[46] Z. Rao, W. Liang, H. Huang, J. Ge, W. Wang, and S. Pan, High sensitivity and rapid response ultraviolet photodetector of a tetragonal $CsPbCl_3$ perovskite single crystal, Opt. Mater. Express **10**, 1374 (2020).

[47] J. N. Wilson, J. M. Frost, S. K. Wallace, and A. Walsh, Dielectric and ferroic properties of metal halide perovskites, APL Mater. **7**, 010901 (2019).

[48] Y. Pu, Z. Dong, P. Zhang, Y. Wu, J. Zhao, and Y. Luo, Dielectric, complex impedance and electrical conductivity studies of the multiferroic $Sr_2FeSi_2O_7$-crystallized glass-ceramics, J. Alloys Compd. **672**, 64 (2016).

[49] A. Ullah, A. Ullah, W. S. Woo, C. W. Ahn, and I. W. Kim, Dielectric spectroscopy of lead-free $Bi_{0.5}(Na_{0.75}K_{0.25})_{0.5}TiO_3$–$BiAlO_3$ ceramics, Ceram. Int. **40**, 11335 (2014).

[50] P. Sengupta, P. Sadhukhan, A. Ray, R. Ray, S. Bhattacharyya, and S. Das, Temperature and frequency dependent dielectric response of $C_3H_7NH_3PbI_3$: A new hybrid perovskite, J. Appl. Phys. **127**, 204103 (2020).

[51] A. Ray, A. Roy, S. Bhattacharjee, S. Jana, C. K. Ghosh, C. Sinha, and S. Das, Correlation between the dielectric and electrochemical properties of TiO_2-V_2O_5 nanocomposite for energy storage application, Electrochim. Acta **266**, 404 (2018).

[52] M. E. Hajlaoui, R. Dhahri, N. Hnainia, A. Benchaabane, E. Dhahri, and K. Khirouni, Conductivity and giant permittivity study of $Zn_{0.5}Ni_{0.5}Fe_2O_4$ spinel ferrite as a function of frequency and temperature, RSC Adv. **9**, 32395 (2019).

[53] J. Liu, C. G. Duan, W. N. Mei, R. W. Smith, and J. R. Hardy, Dielectric properties and Maxwell-Wagner relaxation of compounds A $Cu_3Ti_4O_{12}$ ($A = Ca, Bi_{2/3}, Y_{2/3}, La_{2/3}$), J. Appl. Phys. **98**, 093703 (2005).

[54] K. L. Routray and D. Behera, Structural and dielectric properties of bismuth doped cobalt nano ferrites prepared by sol-gel auto combustion method, IOP Conf. Series: Mater. Sci. Eng. **178**, 012007 (2017).

[55] X. Zheng, S. Wang, J. Wang, W. Hua, J. Zhang, and L. Liu, Long-range and short-range transport dynamics of Li ions in $LiMn_2O_4$, J. Phys. Chem. C **124**, 25254 (2020).

[56] K. Funke and R. Hoppe, Jump-relaxation model yields Kohlrausch-Williams-Watts behaviour, Solid State Ionics **40**, 200 (1990).

[57] A. A. Khamzin, I. I. Popov, and R. R. Nigmatullin, Correction of the power law of ac conductivity in ion-conducting materials due to the electrode polarization effect, Phys. Rev. E **89**, 032303 (2014).

[58] M. B. Bechir, A. Almeshal, and M. H. Dhaou, Interpretation of the giant dielectric constant in the single crystal of the $CH_3NH_3PbBr_3$ perovskite, Mater. Res. Bull. **149**, 111723 (2022).

[59] R. Kumar, P. Srivastava, and M. Bag, Role of A-site cation and x-site halide interactions in mixed-cation mixed-halide perovskites for determining anomalously high ideality factor and the super-linear power law in AC ionic conductivity at operating temperature, ACS Appl. Electron. Mater. **2**, 4087 (2020).

[60] D. P. Almond and A. R. West, Anomalous conductivity prefactors in fast ion conductors, Nature (London) **306**, 456 (1983).

[61] W. Tress, Metal halide perovskites as mixed electronic-ionic conductors: Challenges and opportunities—From hysteresis to memristivity, J. Phys. Chem. Lett. **8**, 3106 (2017).

[62] N. K. Tailor, N. Parikh, P. Yadav, and S. Satapathi, Dielectric relaxation and polaron hopping in $Cs_2AgBiBr_6$ halide double perovskites, J. Phys. Chem. C **126**, 10199 (2022).

[63] D. Ghosh, E. Welch, A. J. Neukirch, A. Zakhidov, and S. Tretiak, Polarons in halide perovskites: A perspective, J. Phys. Chem. Lett. **11**, 3271 (2020).

[64] I. G. Austin and N. F. Mott, Polarons in crystalline and noncrystalline materials, Adv. Phys. **18**, 41 (1969).

[65] A. R. Long, Frequency-dependent loss in amorphous semiconductors, Adv. Phys. **31**, 553 (1982).

[66] A. Ghosh, Frequency-dependent conductivity in bismuth-vanadate glassy semiconductors, Phys. Rev. B **41**, 1479 (1990).

[67] S. R. Elliott, A.c. conduction in amorphous chalcogenide and pnictide semiconductor, Adv. Phys. **36**, 135 (1987).

[68] L. V. Azaroff, *Introduction of Solids* (McGraw-Hill, New York, 1960), p. 395.

[69] Y. Zhao, J. Wang, L. Zhang, S. Liu, D. Zhang, and X. Wang, Large activation energy in aged Mn-doped $Sr_{0.4}Ba_{0.6}Nb_2O_6$ ferroelectric ceramics, RSC Adv. **7**, 26894 (2017).

[70] C. R. Cena, A. K. Behera, and B. Behera, Structural, dielectric, and electrical properties of lithium niobate microfibers, J. Adv. Ceramics **5**, 84 (2016).

[71] C. G. Koops, On the dispersion of resistivity and dielectric constant of some semiconductors at audio frequencies, Phys. Rev. **83**, 121 (1951).

[72] M. Ahmad, M. A. Rafiq, K. Rasool, Z. Imran, and M. M. Hasan, Dielectric and transport properties of bismuth sulfide prepared by solid state reaction method, J. Appl. Phys. **113**, 043704 (2013).

[73] J. Liu, C. G. Duan, W. G. Yin, W. N. Mei, R. W. Smith, and J. R. Hardy, Dielectric permittivity and electric modulus in $Bi_2Ti_4O_{11}$, J. Chem. Phys. **119**, 2812 (2003).

[74] X. Z. Zuo, J. Yang, B. Yuan, D. P. Song, X. W. Tang, K. J. Zhang, X. B. Zhu, W. H. Song, J. M. Dai, and Y. P. Sun, Magnetic, dielectric properties, and scaling behaviors of aurivillius compounds $Bi_{6-x/3}Fe_2Ti_{3-2x}(WCo)_xO_{18}(0 \leqslant x \leqslant 0.15)$, J. Appl. Phys. **117**, 114101 (2015).

[75] G. C. Psarras, E. Manolakaki, and G. M. Tsangaris, Dielectric dispersion and ac conductivity in iron particles loaded-polymer composites, Composites A **34**, 1187 (2003).

[76] P. Thongbai, S. Tangwancharoen, T. Yamwong, and S. Maensiri, Dielectric relaxation and dielectric response mechanism in (Li, Ti)-doped NiO ceramics, J. Phys.: Condens. Matter **20**, 395227 (2008).

[77] S. Havriliak and S. Negami, A complex plane representation of dielectric and mechanical relaxation processes in some polymers, Polymer **8**, 161 (1967).

[78] P. Pal and A. Ghosh, Ionic conduction and relaxation mechanisms in three-dimensional $CsPbCl_3$ perovskite, J. Appl. Phys. **129**, 234102 (2021).

[79] G. Williams and D. C. Watts, Non-symmetrical dielectric relaxation behaviour arising from a simple empirical decay function, Trans. Faraday Soc. **66**, 80 (1970).

[80] K. L. Ngai, Properties of the constant loss in ionically conducting glasses, melts, and crystals, J. Chem. Phys. **110**, 10576 (1999).

[81] F. S. Howell, R. A. Bose, P. B. Macedo, and C. T. Moynihan, Electrical relaxation in a glass-forming molten salt, J. Phys. Chem. **78**, 639 (1974).

[82] S. Summerfield, Universal low-frequency behaviour in the ac hopping conductivity of disordered systems, Philos. Mag. B **52**, 9 (1985).

[83] N. Balkan, P. N. Butcher, W. R. Hogg, A. R. Long, and S. Summerfield, Analysis of frequency-dependent loss data in amorphous silicon and germanium, Philos. Mag. B **51**, L7 (1985).

[84] T. B. Schrøder and J. C. Dyre, Scaling and Universality of ac Conduction in Disordered Solids, Phys. Rev. Lett. **84**, 310 (2000).

[85] B. Roling, A. Happe, K. Funke, and M. D. Ingram, Carrier Concentrations and Relaxation Spectroscopy: New Information from Scaling Properties of Conductivity Spectra in Ionically Conducting Glasses, Phys. Rev. Lett. **78**, 2160 (1997).

[86] A. Ghosh and A. Pan, Scaling of the Conductivity Spectra in Ionic Glasses: Dependence on the Structure, Phys. Rev. Lett. **84**, 2188 (2000).